

The following publication Mei, R., Ma, L., An, L., Wang, F., Xi, J., Sun, H., ... & Wu, Q. (2017). Layered spongy-like O-doped g-C<sub>3</sub>N<sub>4</sub>: an efficient non-metal oxygen reduction catalyst for alkaline fuel cells. *Journal of The Electrochemical Society*, 164(4), F354. is available at <https://doi.org/10.1149/2.1191704jes>

# Layered spongy-like O-doped g-C<sub>3</sub>N<sub>4</sub>: an efficient non-metal oxygen reduction catalyst for alkaline fuel cells

Riguo Mei <sup>a,b,§</sup>, Lei Ma <sup>a,b,§</sup>, Liang An <sup>c</sup>, Fang Wang <sup>a</sup>, Jingjing Xi <sup>a</sup>, Hongyuan Sun <sup>a</sup>, Zhongkuan Luo <sup>a</sup>,  
Qixing Wu <sup>\*,a</sup>

<sup>a</sup> Shenzhen Key Laboratory of New Lithium-ion Batteries and Mesoporous Materials, College of Chemistry and Environmental Engineering, Shenzhen University, 3688 Nanhai Avenue, Nanshan District, Shenzhen, 518060, P.R. China.

<sup>b</sup> Key Laboratory of Optoelectronic Devices and Systems of Ministry of Education and Guangdong Province, College of Optoelectronic Engineering, Shenzhen University, Shenzhen 518060, P.R. China.

<sup>c</sup> Department of Mechanical Engineering, The Hong Kong Polytechnic University, Hung Hom, Kowloon, Hong Kong SAR, China.

**Abstract:** Here we report a polycondensation reaction combined with a solution mixing pathway to synthesize an O-doped graphitic carbon nitride (g-C<sub>3</sub>N<sub>4</sub>) by using melamine and cyanuric acid. Structural and morphological characterizations revealed the successful preparation of O-doped g-C<sub>3</sub>N<sub>4</sub> with a layered spongy-like micro-nanostructure, which favored the enhancement of O<sub>2</sub> adsorption and active sites. The UV-vis spectra and Mott-

---

*Corresponding Author:* \*Qixing Wu, E-mail: [qxwu@szu.edu.cn](mailto:qxwu@szu.edu.cn).

*Author Contributions:* <sup>§</sup> These authors contributed equally to this study and share first authorship.

Schottky analysis indicated that the introduction of oxygen led to a narrow band gap, a negative shift of valence band maximum and an increased electrical conductivity. As a result, the O-doped g-C<sub>3</sub>N<sub>4</sub> exhibited a higher mass activity (14.9 mA/mg<sub>catalyst</sub> at -0.60 V and 1800 rpm) and 60 mV positive shift of half-wave potential toward oxygen reduction reaction (ORR) as well as a better electron transfer efficiency than did the g-C<sub>3</sub>N<sub>4</sub> without oxygen doping. In order to further increase the ORR activity, Ketjen black carbon was incorporated into the O-doped g-C<sub>3</sub>N<sub>4</sub> catalyst to promote the electron transfer. The resulting catalyst showed a comparable ORR activity (a kinetic-limiting current density of 21.5 mA cm<sup>-2</sup> at -0.6 V), excellent stability and remarkable tolerance to methanol as compared with the Pt/C catalyst, indicating its potential application as a non-metal cathode catalyst for the alkaline direct methanol fuel cell.

**Keywords:** graphitic carbon nitride; non-metal catalyst; oxygen reduction reaction; oxygen doping; direct methanol fuel cell

## 1. Introduction

As a non-metal organic semiconductor, the graphitic carbon nitride (g-C<sub>3</sub>N<sub>4</sub>) has received huge attention due to its superior physicochemical stability, attractive electronic structure with an appropriate band position and band gap, tunable structural properties and low cost of raw materials<sup>[1-5]</sup>. These unique characteristics of g-C<sub>3</sub>N<sub>4</sub> make it to be a remarkable catalyst for various applications, including photocatalytic degradation<sup>[6, 7]</sup>, photocatalytic hydrogen

evolution<sup>[8, 9]</sup>, selective organic synthesis<sup>[10, 11]</sup>, oxygen evolution reaction (OER) and oxygen reduction reaction (ORR)<sup>[12-19]</sup>. As a feasible metal-free ORR electrocatalyst, g-C<sub>3</sub>N<sub>4</sub> could present decent reaction sites because it contains relatively high content of pyridinic nitrogen which has been confirmed to be responsibility for ORR<sup>[20-24]</sup>. However, as the specific surface area and electronic conductivity of bulk g-C<sub>3</sub>N<sub>4</sub> are generally low, the actual active sites presented on its surface is quite limited<sup>[25]</sup>. The morphology and structure of g-C<sub>3</sub>N<sub>4</sub>, including macro/micro-morphology, crystal structure and electronic structure can greatly influence its catalytic activity, and thus its morphological and structural control are believed to be crucial.

In the field of photocatalysis, tremendous synthetic techniques and effective modification procedures have been proposed to optimize the morphology and structure of g-C<sub>3</sub>N<sub>4</sub><sup>[26-30]</sup>. Among these methods, supramolecular preorganization based on noncovalent interactions (e.g. hydrogen bonding) seems to emerge as an appealing approach to modify the morphology of g-C<sub>3</sub>N<sub>4</sub><sup>[31-33]</sup>. Shalom et al.<sup>[34]</sup> prepared an ordered and hollow g-C<sub>3</sub>N<sub>4</sub> through supramolecular preorganization of cyanuric acid-melamine complex in ethanol. The as-obtained g-C<sub>3</sub>N<sub>4</sub> exhibited an excellent photocatalytic performance compared with the pristine g-C<sub>3</sub>N<sub>4</sub>. In addition, doping has been demonstrated to be an efficient method to modify the crystal and electronic structures of the bulk g-C<sub>3</sub>N<sub>4</sub><sup>[35-38]</sup>. Ran et al.<sup>[35]</sup> synthesized porous g-C<sub>3</sub>N<sub>4</sub> nanosheets by phosphorus doping and thermal exfoliation to improve their photocatalytic activity. Li et al.<sup>[39]</sup> reported that the O-doped g-C<sub>3</sub>N<sub>4</sub> obtained by a facial H<sub>2</sub>O<sub>2</sub> hydrothermal approach could enhance its photocatalytic reactivity due to the

modification of its electronic structure.

The feasibility of g-C<sub>3</sub>N<sub>4</sub> as a ORR catalyst was first demonstrated by Lyth et al.<sup>[40]</sup> and they found that g-C<sub>3</sub>N<sub>4</sub> exhibited a higher half-wave potential than did carbon black (XC-72R, Cabot). Unfortunately, g-C<sub>3</sub>N<sub>4</sub> alone exhibited an unsatisfied electrocatalytic ORR reactivity and electron transfer ability because of its extremely small electrical conductivity. Hence, incorporation of conductive supports to g-C<sub>3</sub>N<sub>4</sub> became attractive to facilitate the ORR with 4-electron reduction and improve the activity of the catalyst<sup>[25, 41-45]</sup>. Sun et al.<sup>[41]</sup> immobilized g-C<sub>3</sub>N<sub>4</sub> onto the chemically converted graphene by the polymerization method to improve the electrical conductivity. Zheng et al.<sup>[25]</sup> clarified the main hurdles of g-C<sub>3</sub>N<sub>4</sub> toward ORR through theoretical calculations, based on which they demonstrated a competitive non-metal ORR catalyst by incorporating g-C<sub>3</sub>N<sub>4</sub> into mesoporous carbon. Yang et al.<sup>[42]</sup> reported a graphene-based carbon nitride nanosheet by nanocasting and the prepared catalyst exhibited an excellent electrochemical performance due to its improved electrical conductivity, large surface area, increased nitrogen content and small thickness. Tian et al.<sup>[43]</sup> constructed a 3D porous g-C<sub>3</sub>N<sub>4</sub>/reduced graphene oxide by self-assembling to increase the surface area and electrical conductivity of the bulk g-C<sub>3</sub>N<sub>4</sub>. Xu et al.<sup>[45]</sup> reported a facile hydrothermal pathway to synthesize sulfur-doped g-C<sub>3</sub>N<sub>4</sub> with a decoration of graphene quantum dots and a superior ORR performance was achieved as compared with the undecorated g-C<sub>3</sub>N<sub>4</sub>.

The above literature review indicated that most of previous studies on g-C<sub>3</sub>N<sub>4</sub> catalysts for ORR focused on the incorporation of conductive supports and relatively few work was

reported regarding to the structural modification of bulk g-C<sub>3</sub>N<sub>4</sub> to increase its electroactivity. Meanwhile, the advantages of supramolecular frameworks and doping have been proven effective in photocatalysis and thus it would be interesting to extend them to the electrocatalysis of ORR. In this work, a polycondensation reaction combined with a solution mixing pathway was proposed to synthesize the O-doped g-C<sub>3</sub>N<sub>4</sub> with a layered spongy-like micro-nanostructure by using melamine and cyanuric acid as raw materials. The preparation of O-doped g-C<sub>3</sub>N<sub>4</sub> involved two steps: 1) formation of hexagonal plate-like melamine-cyanuric acid (M-CA) frameworks with supramolecular lattice through a simple solution mixing; 2) partial substitution of nitrogen by oxygen during polycondensation. It was expected that the unique structure of the synthesized O-doped g-C<sub>3</sub>N<sub>4</sub> was beneficial for enhancing the electrical conductivity, oxygen adsorption and exposure of active sites for ORR. The structure and morphology of the prepared catalysts were analyzed by a series of characterizations including scanning electron microscopy (SEM), high-resolution transmission electron microscopy (HR-TEM), atomic force microscopy (AFM), X-ray diffraction (XRD), Fourier transform infrared spectroscopy (FT-IR), Raman spectrum, X-ray photoelectron spectroscopy (XPS) and UV-vis spectroscopy. In addition, the electrocatalytic activities of O-doped g-C<sub>3</sub>N<sub>4</sub> before and after incorporation of conductive carbon black were also evaluated systematically.

## 2. Experimental

**2.1 Synthesis of O-gCN and O-gCN/KB catalysts.** As depicted in Scheme 1a, O-doped g-C<sub>3</sub>N<sub>4</sub> was synthesized through a polycondensation reaction combined with a solution mixing pathway by using melamine and cyanuric acid in deionized water as starting materials. Firstly, 1.26 g melamine (Aladin, 99%) and 1.29 g cyanuric acid (Aladin, 98%) were respectively dissolved into 100 ml hot water (80 °C) under continuous stirring. After completely dissolved, the melamine solution was slowly poured into cyanuric acid solution and white precipitate was quickly produced. Then, the white suspension was filtered and washed by deionized water and ethanol. To obtain precursor powder (M-CA complex), the filter cake was dried at 80 °C for 12 h under vacuum. Lastly, the O-doped g-C<sub>3</sub>N<sub>4</sub> (O-gCN) was synthesized after polycondensation at the temperature of 550 °C for 5 h under N<sub>2</sub> atmosphere. Scheme 1b presents the corresponding chemical structure of melamine, cyanuric acid, M-CA supramolecular and O-doped g-C<sub>3</sub>N<sub>4</sub>. For comparison, the g-C<sub>3</sub>N<sub>4</sub> without oxygen doping (gCN) was also synthesized via polycondensing the mixture of melamine and cyanuric acid (M-CA mixture), which was obtained by manual grinding in an agate mortar.

In order to improve the electrical conductivity of O-gCN, conductive carbon black was incorporated into the O-gCN to promote electron transfer (ET) ability. Ketjen black EC 600JD (KB) was chosen as the carbon support because of its excellent properties, including good electrical conductivity, large specific surface area of ~1200 m<sup>2</sup> g<sup>-1</sup> and good corrosion resistance, which were beneficial to improve the ORR activity and stability. Carbon supported O-doped g-C<sub>3</sub>N<sub>4</sub> catalysts were synthesized through a simple process. Typically, O-gCN and KB (1:1 wt. %) were ultrasonically dispersed in deionized water for 15 min,

followed by filtering and washing. Then the filter cake was dried at 80 °C for 12 h under vacuum and a mixture of O-gCN and KB (O-gCN/KB mixture) was obtained. The O-gCN/KB mixture was further treated at the temperature of 550 °C for 1 h to attain the O-gCN/KB complex catalyst (O-gCN/KB complex).

**2.2 Characterizations.** The crystalline structures of precursors and products were investigated by an X-ray diffractometer (Ultima IV, Japan) at a step size of 0.02 °, a count time of 0.6 s per step and 2theta between 10 and 80 ° with Cu K $\alpha$  radiation under 40 kV and 40 mA. SEM images and energy dispersive spectrometer (EDS) were obtained after aurum coating by using a field emission scanning electron microscope (JSM-7800F). TEM images were obtained by using a field emission transmission electron microscope (JEM-2100F). MultiMode-8 (Germany Bruker Company) is used for AFM characterizations. N<sub>2</sub> adsorption and desorption isotherms were attained from a BELSORP-max system (Microtrac BEL Japan, Inc.) at liquid N<sub>2</sub> temperature. XPS characterizations were carried out by an ESCALABMK II X-ray photoelectron spectrometer using Al K $\alpha$  radiation and the binding energy was corrected by using C 1s (284.8 eV) as a reference. The XPS source was calibrated before each measurement to achieve the accuracy required in the analysis and the fitting parameters of O1s, C1s and N1s were listed in the Table S3, S4 and S5, respectively. FT-IR data were collected on FT-IR Spectrometer (Spectrum One Version B, America). Raman data were collected from Raman spectroscopy (Renishaw Raman Microscope, 532 nm HeNe Laser). The diffuse reflection spectrum (DRS) was recorded in a UV-visible spectrophotometer (Shimadzu, Japan). The electrical conductivity was measured by a four-

probe conductivity meter (RTS-9, China) at room temperature. To perform the conductivity test, 1.0 g powder was pressed at 15 MPa to attain a coin-like platelet with a diameter of 1 cm and a thickness of about 0.35 cm.

**2.3 Electrocatalytic Measurements.** To prepare the catalyst ink, 1.2 mg g-C<sub>3</sub>N<sub>4</sub> catalyst with 1000  $\mu$ L ethanol, 900  $\mu$ L deionized water and 100  $\mu$ L Nafion solution (5 wt. %) were mixed ultrasonically for 30 min. Then, 20  $\mu$ L suspension of catalyst ink was pasted onto the working electrode of a rotating disk electrode (RDE, area: 0.07 cm<sup>2</sup>), resulting in a loading of 170  $\mu$ g cm<sup>-2</sup> catalyst. For O-gCN/KB catalysts, 2.4 mg O-gCN/KB mixture or complex was dispersed in 1000  $\mu$ L ethanol, 900  $\mu$ L deionized water and 100  $\mu$ L 5 wt. % Nafion solution for 30 min. After ultrasonic dispersion for 1 h, 10  $\mu$ L suspension of catalyst ink was loaded onto the RDE, resulting in an O-gCN/KB catalyst loading of 170  $\mu$ g cm<sup>-2</sup>.

For comparison, a 1.2 mg mL<sup>-1</sup> suspension of commercial Pt/C (40 wt. % Pt, HiSPEC 4000, Johnson Matthey) was obtained according to the same procedure described above and then 10  $\mu$ L catalyst ink was added to the RDE, resulting in a Pt/C loading of 170  $\mu$ g cm<sup>-2</sup>.

All the electrochemical measurements were performed under room temperature (25 °C). Cyclic voltammetry (CV), linear sweep voltammetry (LSV) and electrode kinetics studies were performed in a three-electrode electrochemical cell using a RDE system. The reference electrode was an Ag/AgCl in saturated KCl solution and the counter electrode was platinum net. The data were recorded using an electrochemical workstation (Metrohm PGSTAT302N Autolab, Netherlands). An O<sub>2</sub> saturated electrolyte was prepared by purging O<sub>2</sub> (99.999%) into the electrolyte solution for 30 min and a continuous flow of O<sub>2</sub> was kept during ORR

measurements. For comparison, CVs of various catalysts were also conducted under an N<sub>2</sub> (99.99%) environment.

Mott-Schottky analysis was carried out at a potential range of -0.6-0.2 V vs. Ag/AgCl with a frequency of 10 kHz and an amplitude of 10 mV in 0.1 M KOH. CV characterization of catalysts was carried out in N<sub>2</sub> or O<sub>2</sub>-saturated KOH (0.1 and 1 M) electrolyte with a scan rate of 10 mV s<sup>-1</sup> among -0.6 V and 0.2 V. In RDE tests, LSV characterization was carried out in O<sub>2</sub>-saturated 1 M KOH electrolyte with a scan rate of 5 mV s<sup>-1</sup> among -0.6 to 0.2 V under various rotation rates (600, 1200, 1800, 2400 and 3000 rpm). Electrochemical impedance spectra (EIS) was carried out in O<sub>2</sub>-saturated 1 M KOH electrolyte at a bias potential of -0.2 V vs. Ag/AgCl with a perturbation amplitude of 10 mV and a frequency ranging from 10<sup>5</sup> to 0.1 Hz. In order to further investigate dynamics properties of ORR for O-gCN/KB catalysts, CV characterizations were carried out in O<sub>2</sub>-saturated 1 M KOH electrolyte by different scan rates (100, 80, 60, 40, 20 mV/s) with potentials ranging from -0.6 to 0.2 V. The accelerated degradation test (ADT)<sup>[21, 46]</sup> was conducted in N<sub>2</sub>-saturated 1 M KOH with a scan rate of 50 mV s<sup>-1</sup> among -0.6 to 0.2 V for 10000 cycles. In order to further investigate the stability of O-gCN during ORR process, the composition of O-gCN after ADT were characterized by XPS again. The corresponding Pt/C data were recorded with the same test conditions as those of O-gCN/KB catalysts. All data were corrected for an ohmic drop of ~7.8 Ω or ~68 Ω, respectively, in 1 or 0.1 M KOH<sup>[47]</sup>.

### 3. Results and discussion

### 3.1 Characterizations of structure and composition

As shown in Figure 1a, M-CA complex, formed by a solution mixing of melamine and cyanuric acid, reveals a hexagonal plate-like structure, in agreement with the hypothesis that the M-CA complex is tended to form a hexagonal network through the formation of hydrogen bonds<sup>[48]</sup>. Compared with the planar H-bond interaction, the  $\pi$ - $\pi$  interactions between layered M-CA supramolecular are preferentially broken under ultrasonic exfoliation. As a result, one can directly observe a few layered M-CA supramolecular frameworks by using an AFM. Figure 1g shows 2-3 layered M-CA supramolecular frameworks with a thickness of 1.4 nm. The irregular M-CA supramolecular frameworks with many pores are likely to demonstrate that some H-bonds of M-CA supramolecular are broken under ultrasonic exfoliation. After polycondensation reaction, the M-CA supramolecular frameworks transfer into g-C<sub>3</sub>N<sub>4</sub> frameworks. Obvious changes of the morphology are observed from SEM images. Figure 1b shows that the synthesized g-C<sub>3</sub>N<sub>4</sub> product has a spongy-like micro-nanostructure, which is comprised of layered g-C<sub>3</sub>N<sub>4</sub> frameworks. A few layered g-C<sub>3</sub>N<sub>4</sub> frameworks, obtained from spongy-like g-C<sub>3</sub>N<sub>4</sub> by ultrasonic exfoliation, are detected by TEM and AFM. 2D g-C<sub>3</sub>N<sub>4</sub> nanosheets with a thickness of 1.5 nm are clearly observed from Figure 1c and Figure 1h. The formation of spongy-like micro- nanostructure with layered g-C<sub>3</sub>N<sub>4</sub> nanosheets is probably attributed to the release of gas molecules, which causes the structural expansion of layered M-CA supramolecular frameworks. In contrast, the g-C<sub>3</sub>N<sub>4</sub> product derived from M-CA mixture shows a cavity structure with irregular shapes due to the release of gas from the internal of irregular particles during the polycondensation reaction (Figure 1d). Compared

with layered spongy-like g-C<sub>3</sub>N<sub>4</sub>, the cavity-structured g-C<sub>3</sub>N<sub>4</sub> is seriously aggregated as shown in Figure 1e and 1f. Consequently, the specific surface area of the spongy-like g-C<sub>3</sub>N<sub>4</sub> increased up to 58.3 m<sup>2</sup> g<sup>-1</sup>, roughly 2.5 times higher than that of the cavity-structured g-C<sub>3</sub>N<sub>4</sub> (Figure S1 and Table 1). It is believed that the hierarchical structures of spongy-like g-C<sub>3</sub>N<sub>4</sub> with layered nanosheets can not only provide more active sites, but also facilitate the access of electrolyte and O<sub>2</sub>, resulting in a higher ORR reactivity. By using elemental analysis (Table 1) and combined SEM-EDS (Figure S3), it can be found that extra oxygen atoms are detected in the g-C<sub>3</sub>N<sub>4</sub> sample derived from M-CA complex, probably suggesting the successful introduction of oxygen atoms into g-C<sub>3</sub>N<sub>4</sub> through M-CA supramolecular lattice. A possible chemical reaction pathway shown in Figure 1i is proposed to interpret oxygen-doping in the supramolecular frameworks. It is hypothesized that the melamine and cyanuric acid in M-CA supramolecular lattice would migrate to form a favorable reaction location due to molecular thermal motion during thermal treatment. Subsequently, oxygen atom can be directly incorporated into g-C<sub>3</sub>N<sub>4</sub> during a classical condensation scheme of carbon nitride <sup>[49]</sup>.

XRD and FTIR are applied to further investigate structural variation from M-CA complex to O-doped g-C<sub>3</sub>N<sub>4</sub>. Figure 2a shows the XRD patterns of M-CA complex, M-CA mixture, and their polycondensation products. The appearance of new peaks for M-CA complex compared with M-CA mixture can be viewed as a solid evidence for the occurrence of new arrangement. The high crystallinity noted in the XRD pattern of M-CA complex strongly suggests that the M-CA complex possesses a hexagonal structure. According to the

hexagonal structure model of M-CA supramolecular complex proposed by Rao<sup>[48]</sup>, three obvious peaks at 10.67, 11.90 and 18.41° may be assigned to (100), (010), and (110) of the in-planar pattern, respectively. Apparently, another two peaks at 21.41 and 23.80° are precisely corresponding to crystal faces of (200) and (020), respectively. Furthermore, the strongest diffraction peaks observed at 27.92° is well assigned to the lamellar stacking peak of (002) crystal plane, supporting the observed sheet-like structure (see Figure 1a). In addition, no peaks of melamine or cyanuric acid have been detected in M-CA complex, indicating a complete reaction of melamine and cyanuric acid through the solution mixing process. Obviously, the XRD pattern of M-CA mixture presents no other diffraction peaks except for those of melamine and cyanuric acid, confirming a simple physical mixing of melamine and cyanuric acid. For both gCN and O-gCN samples, two characteristic peaks located at around 12.9 and 27.3° give crystalline interplanar spacing of 6.80 and 3.26 Å, corresponding to the (110) interplanar distance between heptazine units and the interlayer distance of stacking g-C<sub>3</sub>N<sub>4</sub> sheets, respectively. It is notable that, with a close observation (Figure 2b), the full width at half maximum (FWHM) of (110) peak for O-gCN enlarges from 0.45 to 0.6° compared with gCN. Moreover, the (002) peak in O-gCN shifts from 27.43 to 27.23° compared with that of gCN, indicating that the layer distance decreased from 3.26 to 3.24 Å. These results could be interpreted as the lattice distortion and the delocalization of  $\pi$ -conjugated bonds due to the introduction of oxygen heteroatoms.

Another evidence supporting the construction of the M-CA complex is presented in Figure 2c. It is known that C=O stretching vibration of cyanuric acid and the triazine ring vibration

of melamine will be influenced by the hydrogen bonding interaction of cyanuric acid and melamine<sup>[34]</sup>. Compared with M-CA mixture, M-CA complex gives a red shift of C=O stretching vibration from 1691 to 1734  $\text{cm}^{-1}$ , and a blue shift of triazine ring vibration from 809 to 769  $\text{cm}^{-1}$ . After polycondensation reaction, the spectrum of gCN derived from M-CA complex shows extra C=O stretching vibration compared with that of gCN derived from M-CA mixture, providing a strong evidence of oxygen doping in gCN derived from M-CA complex. With a close observation in Figure 2d, several bands are observed within 1200-1600  $\text{cm}^{-1}$  for both gCN and O-gCN, corresponding to the CN heterocycles stretching modes<sup>[50]</sup>. In addition, the breathing mode of the triazine units is also detected at 809  $\text{cm}^{-1}$  for both gCN and O-gCN.

Further evidence of oxygen doping in g- $\text{C}_3\text{N}_4$  is determined by XPS. In order to eliminate the influence of ambient  $\text{H}_2\text{O}$  and  $\text{O}_2$ , the sample surface is treated by  $\text{Ar}^+$  etching for 60 s. As shown in Figure 3a, the O-gCN shows O 1s core level, while no signal related to 1s core level is observed for the gCN. For the O 1s spectrum, only O-doped sample exhibits O 1s core level at 531.6 eV, which should be ascribed to the creation of C-O-C species. In the C 1s spectrum, both the gCN and O-gCN contain graphitic carbon (C-C) and  $\text{sp}^2$ -hybridized carbon in the N-containing aromatic ring (N-C=N), which located at 284.6 and 288.0 eV, respectively. Besides, the O-gCN shows a new carbon species at 285.9 eV which can be assigned to the C-O species, consistent with the results of FTIR (Figure 2c). The formation of C-O species on the O-gCN suggests that  $\text{sp}^2$ -hybridized carbon may be bonded with oxygen atoms. Meanwhile, all the g- $\text{C}_3\text{N}_4$  catalysts show similar N 1s spectra with four nitrogen

species (C=N, 397-399 eV; C<sub>3</sub>-N, 400 eV; N-H<sub>2</sub>, 401-403 eV; and C<sub>6</sub>N<sub>7</sub>, 404-405 eV). Additionally, no signal related to N-O species is observed for O-gCN, indicating that the doped oxygen atoms substitute nitrogen atoms rather than carbon atoms. In comparison with gCN, O-gCN presents an increased C/N atomic ratio and decreased intensity ratio of N(sp<sup>2</sup>)/N(sp<sup>3</sup>), further supporting the substitution of nitrogen atom by oxygen atom. The weight content of oxygen element obtained from elemental analysis is 3.24 wt. % for O-gCN, closed to the results from EDS and XPS analysis. The contents of different C and N species for O-gCN and gCN from XPS analysis are listed in Table 2. It is worth mentioning that after oxygen doping, the pyridinic-N content of O-gCN is higher than that of gCN. As pyridinic-N may likely contribute to the formation of active sites for ORR<sup>[21, 24]</sup>, an increased pyridinic-N content of O-gCN is favorable for improving its ORR performance.

### **3.2 band structure analysis**

UV/Vis light absorption spectra and Mott-Schottky plots are applied to study the influence of oxygen doping on the band structure of g-C<sub>3</sub>N<sub>4</sub>. UV-vis spectra (Figure 4a) show that the absorption edge of the O-gCN shifts from 444 nm to 480 nm compared with the gCN. Meanwhile, Tauc plots obtained from the Kubelka-Munk function reveal a decrease in the bandgap energy of O-gCN to 2.58 eV as compared to 2.79 eV for gCN (inset in Figure 4a), indicating an increase of electron conductivity for O-gCN, consistent with the previous report<sup>[39]</sup>. Mott-Schottky plots refer to the apparent capacitance as a function of potential in different frequency ranges. As shown in Figure 4b and 4c, both gCN and O-gCN exhibit positive slopes in the Mott-Schottky plots, implying n-type characteristic of semiconductors.

Moreover, the Mott-Schottky plots of gCN and O-gCN give the same x-intercept at frequencies of 100, 125, 150, 175 and 200 kHz, thereby suggesting the flat potentials are independent on frequencies. According to the x-intercept, the flat potentials ( $V_{fb}$ , vs. Ag/AgCl, pH=7.0) of O-gCN and gCN are estimated to be -1.21 and -1.38 eV, respectively. For n-type semiconductors, the estimated flat potentials from Mott-Schottky plots are equal to conduction band maximum (CBM) and thus the CBM of O-gCN positively shifts about 0.17 eV compared with that of gCN. Such a positive shift may be arisen from the high electronegativity of impurity oxygen atoms so that redistribution and delocalization of additional electrons would proceed to form a defect-related state below the CBM of the gCN [39, 51]. According to their band gaps, the valance band maximum (VBM) of O-gCN and gCN could be calculated to be approximately 1.36 and 1.41 eV respectively. Figure 4d shows schematic band structures of the O-gCN and gCN together with the potentials for  $H^+$  and oxygen reduction reactions. Clearly, the VBM of O-gCN is about 0.05 eV smaller than that of gCN, probably because its atomic states are hybridized after oxygen doping via substitution of nitrogen atoms by oxygen atoms or structural distortion. It is believed that a narrower bandgap, a VBM negative shift and a higher electron conductivity of the O-gCN can facilitate the electron transfer process during ORR.

### **3.3 Measurements of electrocatalytic performance**

The electrocatalytic activities for ORR on g-C<sub>3</sub>N<sub>4</sub> catalysts are evaluated by using RDE. Figure 5a shows the CVs of gCN and O- gCN in N<sub>2</sub>- or O<sub>2</sub>-saturated 1 M KOH solution with a rotating rate of 1800 rpm. The CV curves recorded for gCN and O-gCN in O<sub>2</sub>-saturated 1M

KOH solution have an obvious ORR peak within the potentials of -0.6-0.2 V. Conversely, there are no observable peaks for gCN and O-gCN in N<sub>2</sub>-saturated 1 M KOH solution. These results demonstrate that gCN and O-gCN possess a noticeable ORR activity and have great potential as metal-free electrocatalysts for ORR. Moreover, O-gCN has a relatively higher peak potential and peak current compared with gCN, indicating that O-gCN possesses a higher catalytic activity than does gCN. Consistent results are obtained from a series of LSV tests on a RDE at various rotating rates from 600 to 3000 rpm. The O-gCN electrode reveals a higher half-wave potential and larger ORR current density than does the gCN electrode (Figure 5b). Also, from the diffusion-limiting current densities, it can be inferred that the O-gCN yields a higher mass activity (14.9 mA/mg<sub>catalyst</sub> at -0.60 V and 1800 rpm) than does the gCN (5.4 mA/mg<sub>catalyst</sub>). The turnover frequency (TOF) is an important parameter to characterize the kinetics of the ORR for active moieties present in the catalyst materials. The TOFs for the ORR at defined operating conditions are estimated based on 4e<sup>-</sup> ORR process and the resulting TOFs of gCN and O-gCN are 0.0004 and 0.001 s<sup>-1</sup> (See Supplementary Materials), respectively. Besides, it is observed in Figure 5b that the diffusion-limiting current densities of gCN and O-gCN electrodes increase with an increase in rotation rates, suggesting the oxygen diffusion-limiting reaction kinetics. The improved ET efficiency of O-gCN is further confirmed from the electron transfer number (n) calculated by the Koutechy-Levich equation. As shown in Figure 5c, the numbers of electron transfer for gCN and O-gCN are slightly changed with the variation of potentials, indicating a complex ORR mechanism for both gCN and O-gCN. Moreover, O-gCN exhibits a larger electron transfer

number compared with gCN, confirming the improved ET efficiency of O-gCN. Besides, the Koutecky-Levich plots (inset of Figure 5c) show nearly linear dependence of  $J^{-1}$  and  $\omega^{-1/2}$ , demonstrating the oxygen diffusion limiting reaction kinetics for ORR. The Tafel plots presented in Figure 5d show similar slopes for O-gCN (53 mV/dec) and gCN (69 mV/dec), which are similar to those of catalysts involving analogous active sites with the carbon atoms adjacent to the pyridinic-N<sup>[52]</sup>.

Compared with gCN, the enhancement of electron transfer number for O-gCN is probably attributed to the O-containing active moieties, which may proceed via 4e<sup>-</sup> ORR process due to the redistribution of electron states and delocalization among the big  $\pi$ -bonds of the O-containing active moieties. Based on the spectroscopic and electrochemical analyses, one can see that the layered spongy-like structure of O-gCN is beneficial for the ORR reactivity due to its higher BET surface and unique layered structure for O<sub>2</sub> adsorption and transfer. Moreover, the introduction of oxygen atoms in g-C<sub>3</sub>N<sub>4</sub> could tune the band structure, which leads to a narrower bandgap, a VBM negative shift and a higher electron conductivity. As a result, the electron transfer of O-gCN is effectively accelerated to improve its ORR performance.

Although O-gCN alone exhibits a promising activity toward alkaline ORR, it is still uncompetitive with other metal-free ORR catalysts. According to the conductivity tests, the conductivity of O-gCN is small than 10<sup>-5</sup> S cm<sup>-1</sup>, which is the lower limit of the conductivity meter. It is well understood that the poor electrical conductivity would limit its ET and catalyst utilization, thus leading to a poor ORR activity. In order to improve the electrical

conductivity of O-gCN, KB carbon black is introduced as support for O-gCN to promote ET. As a result, the conductivity of O-gCN/KB composites increases by at least 6 orders compared with that of O-gCN. Moreover, the conductivity of O-gCN/KB complex is  $98.5 \text{ S cm}^{-1}$ , 7 times larger than that of O-gCN/KB mixture.

The electrocatalytic performances of O-gCN/KB catalysts are investigated by various electrochemical measurements. It can be seen in Figure 6a that KB shows no ORR peak and O-gCN shows a weak ORR peak at  $-0.28 \text{ V}$ , whereas O-gCN/KB mixture and O-gCN/KB complex both present a strong cathodic peak. As no characteristic peaks are observed for O-gCN/KB mixture and O-gCN/KB complex in  $\text{N}_2$ -saturated  $1 \text{ M KOH}$  solution (Figure S5), such strong peaks should be attributed to the ORR process. Clearly, it can be inferred from Figure 6a that the incorporation of KB into O-gCN catalyst results in a salient improvement of ORR activity. From the results of LSV (Figure 6b), one can further see that O-gCN/KB complex exhibits a higher half-wave potential and larger current density than do KB, O-gCN and O-gCN/KB mixture electrodes, consistent with the results of the CV measurements. Moreover, it is also found that limiting current density and the half-wave potential of O-gCN/KB complex are comparable with those of Pt/C catalysts, indicating its potential application as a highly efficient, cost-effective and non-metal ORR electrocatalyst. In addition, the Tafel plots in Figure S6a show that O-gCN/KB complex presents a smaller slope ( $44 \text{ mV dec}^{-1}$ ) than does O-gCN/KB mixture ( $48 \text{ mV dec}^{-1}$ ), consistent with its higher kinetic reactivity. Furthermore, as shown in Figure S6b, O-gCN/KB complex exhibits a

smaller charge transfer resistance than does O-gCN/KB mixture, further confirming an enhancement of ET efficiency.

In order to investigate the ET mechanism, a series of LSVs at different electrode rotation rates for O-gCN/KB mixture (Figure 6c) and O-gCN/KB complex (Figure 6d) are obtained to calculate the electron transfer number ( $n$ ) and kinetic-limiting current density ( $J_k$ ) by the Koutechy-Levich equation. As shown in Figure S7, the electron transfer number ( $n$ ) of O-gCN/KB complex is larger than those of O-gCN/KB mixture in the potentials of -0.6-0.3 V. Moreover, the kinetic-limiting current density of O-gCN/KB complex is calculated to be 21.5 mA cm<sup>-2</sup> at -0.6 V, substantially larger than that of O-gCN/KB mixture (13.3 mA cm<sup>-2</sup>). Such variations in  $n$  and  $J_k$  between O-gCN/KB complex and mixture can be understood by Figure S4: O-gCN and KB in O-gCN/KB complex combine more tightly to form more O-gCN/KB interfaces than does O-gCN/KB mixture, leading to a higher ET efficiency due to a shorter electron tunneling distance. In addition, it is also seen in Figure S7a that the electron transfer number increases with a decrease of potential from -0.3 to -0.6 V for both O-gCN/KB mixture and O-gCN/KB complex, indicating a kinetic-limiting ET process for ORR.

To better study the kinetic properties of ORR, a series of CV tests for O-gCN/KB mixture (Figure S8a) and O-gCN/KB complex (Figure S8b) are conducted at different potential sweep rates in O<sub>2</sub>-saturated 1 M KOH solution. Obviously, it is seen that the peak currents ( $i_p$ ) increase and the peak potentials ( $E_p$ ) negatively shift with an increase of potential sweep rate, which are well demonstrated in the literature <sup>[53]</sup>. For a completely irreversible reaction, the

relationship between peak current density ( $i_p$ ) and peak potential ( $E_p$ ) in CVs at 25 °C can be depicted by the following equations<sup>[54]</sup>.

$$i_p = (0.227nFc_0k_s)\exp\left[\left(\frac{\alpha F}{RT}\right)(E_p - E^0)\right] \quad \text{Eq. 1}$$

$$\ln i_p = \ln(0.227nFc_0k_s) - \left(\frac{\alpha F}{RT}\right)(E_p - E^0) \quad \text{Eq. 2}$$

where,  $i_p$  represents the peak current density ( $\text{A cm}^{-2}$ ),  $E_p$  represents the peak potential (V vs. Ag/AgCl),  $E^0$  represents the equilibrium potential (V vs. Ag/AgCl);  $k_s$  represents the rate constant ( $\text{cm s}^{-1}$ );  $n$  is the electron transfer number, for ORR,  $n=4$ ;  $F$  is the Faraday constant ( $96485 \text{ C mol}^{-1}$ );  $R$  is the gas constant ( $8.314 \text{ J mol}^{-1} \text{ K}^{-1}$ );  $T$  is the ambient temperature (25 °C);  $c_0$  is the bulk concentration of oxygen ( $1.2 \times 10^{-6} \text{ mol cm}^{-3}$ ); and  $\alpha$  is the charge transfer coefficient. According to the insets in Figure S8a and S8b, the ORR peak potential ( $E_p$ ) and  $\ln(i_p)$  with various potential sweep rates are in a good agreement with Eq. 2: the linear coefficient of determination ( $R^2$ ) between ( $E_p - E^0$ ) and  $\ln(i_p)$  are 0.998 and 0.994, respectively, for O-gCN/KB mixture and O-gCN/KB complex. Hence, it is valid to estimate the rate constants by Eq. 1. The O-gCN/KB complex reveals an estimated rate constant ( $k_s$ ) of  $9.0 \times 10^{-5} \text{ cm s}^{-1}$ , much higher than that of O-gCN/KB mixture ( $2.9 \times 10^{-9} \text{ cm s}^{-1}$ ), which indicates a higher kinetic reactivity of O-gCN/KB complex.

The stability of O-gCN/KB mixture, O-gCN/KB complex, and Pt/C are evaluated by ADT experiments. As shown in Figure S9, the CV curves for both O-gCN/KB mixture and O-gCN/KB complex are almost overlapped before and after ADT, indicating that O-gCN/KB mixture and O-gCN/KB complex possess a superior stability compared with commercial Pt/C, which presents an observable decline for ORR peak. Moreover, the half-wave potentials

shift 9, 4 and 30 mV for O-gCN/KB mixture, O-gCN/KB complex, and Pt/C, respectively. The excellent stability of O-gCN/KB complex arises not only from the stable structures of O-gCN catalyst and KB support but also from the intimate contact and more homogeneous interaction between O-gCN and KB. In addition, to further investigate the stability of O-gCN in the alkaline environment, the Raman spectroscopy has been used at the first attempt. Unfortunately, no detectable peaks of C-O bonds can be obtained from Raman spectroscopy due to their strong fluorescence effect (Figure S2). Then, we have measured the composition of O-gCN after ADT by XPS and the results are shown in Figure S10. It is found that the oxygen and its derived species are still existed in the O-gCN sample after ORR process. The contents of oxygen element (Table S1) and oxygen-containing species (Table S2) are found to be nearly unchanged for the O-gCN after ORR process, suggesting its relatively good stability even in alkaline media.

Figure 6e show the chronoamperometry results of O-gCN/KB mixture, O-gCN/KB complex and Pt/C. As shown in Figure 6e, O-gCN/KB complex exhibits the highest short-term stability with a low degradation rate compared with O-gCN/KB mixture and commercial Pt/C. The current retention ratio of O-gCN/KB complex remains 98.5% after 8 h, which is much higher than those of O-gCN/KB mixture and commercial Pt/C. The sensitivity to methanol poisoning is critical for catalysts of direct methanol fuel cells. To investigate the sensitivities of O-gCN/KB catalysts to methanol poisoning, the chronoamperometric tests of various catalysts are interrupted by adding 1 mL 4 M methanol solution into the electrolyte. As expected, the cathodic ORR currents at -0.3 V of both O-gCN/KB mixture and complex

remain nearly unchanged with negligibly small drops after addition of methanol (Figure 6f), suggesting their strong tolerance against methanol. In contrast, the cathodic current of commercial Pt/C catalyst drops by 3.5% immediately after the introduction of methanol. Moreover, a further decline of the cathodic current of Pt/C catalyst is also observed, implying severe poisoning on Pt/C catalysts by methanol. The remarkable methanol tolerance ability of O-gCN/KB complex demonstrates its potential use as a non-metal cathode catalyst for direct methanol fuel cells in alkaline medium.

#### **4. Conclusions**

In summary, derived from M-CA supramolecular lattice, O-gCN with layered spongy-like structure is successfully synthesized through a facile and low-cost approach. As a metal-free electrocatalyst for ORR, the layered spongy-like structure of O-gCN is benefit for O<sub>2</sub> adsorption and transfer. Moreover, the introduction of oxygen atoms in g-C<sub>3</sub>N<sub>4</sub> tunes the band structure so that a narrower bandgap, a negative shift of VBM and a higher electron conductivity can be achieved, all of which facilitates the electron transfer. Therefore, the O-gCN exhibits an improved ORR activity and ET efficiency compared with O-gCN. After incorporation of KB carbon black as a conductive support, the resulting O-gCN/KB complex reveals a comparable ORR reactivity, excellent stability and remarkable poisoning tolerance compared with commercial noble Pt/C catalysts, demonstrating its great potential as an alternative metal-free catalyst for alkaline direct methanol fuel cell.

## Acknowledgments

This work was supported by the National Natural Science Foundation of China (No. 51306125), Shenzhen Science and Technology Fund (KQCX20140519105122378 and JCYJ20150324141711693) and Natural Science Foundation of SZU (No. 827-000015).

## References

1. Y. H. Qi, L. Liu, Y. H. Liang, J. S. Hu and W. Q. Cui, *Prog Chem*, **27**, 38 (2015).
2. S. Ye, R. Wang, M. Z. Wu and Y. P. Yuan, *Appl Surf Sci*, **358**, 15 (2015).
3. Z. W. Zhao, Y. J. Sun and F. Dong, *Nanoscale*, **7**, 15 (2015).
4. Y. Zheng, L. H. Lin, B. Wang and X. C. Wang, *Angew Chem Int Edit*, **54**, 12868 (2015).
5. G. Algara-Siller, N. Severin, S. Y. Chong, T. Bjorkman, R. G. Palgrave, A. Laybourn, M. Antonietti, Y. Z. Khimyak, A. V. Krashennnikov, J. P. Rabe, U. Kaiser, A. I. Cooper, A. Thomas and M. J. Bojdys, *Angew Chem Int Ed Engl*, **53**, 7450 (2014).
6. M. Zhang, W. J. Jiang, D. Liu, J. Wang, Y. F. Liu, Y. Y. Zhu and Y. F. Zhu, *Appl Catal B-Environ*, **183**, 263 (2016).
7. X. Liu, X. L. Wu, Z. Long, C. Zhang, Y. Q. Ma, X. H. Hao, H. Y. Zhang and C. P. Pan, *J Agr Food Chem*, **63**, 4754 (2015).
8. J. Jiang, J. G. Yu and S. W. Cao, *Journal of colloid and interface science*, **461**, 56 (2016).
9. X. B. Li, A. F. Masters and T. Maschmeyer, *Chemcatchem*, **7**, 121 (2015).
10. X. Chen, J. Zhang, X. Fu, M. Antonietti and X. Wang, *J Am Chem Soc*, **131**, 11658 (2009).
11. S. Verma, R. N. Baig, M. N. Nadagouda and R. S. Varma, *Acs Sustain Chem Eng*, **4**, 1094 (2016).
12. W. B. Luo, S. L. Chou, J. Z. Wang, Y. C. Zhai and H. K. Liu, *Small*, **11**, 2817 (2015).
13. W. Gu, L. Hu, J. Li and E. Wang, *Acs Appl Mater Inter* (2016).
14. W. Yang, T.-P. Fellinger and M. Antonietti, *J Am Chem Soc*, **133**, 206 (2010).
15. H. Tao, C. Yan, A. W. Robertson, Y. Gao, J. Ding, Y. Zhang, T. Ma and Z. Sun, *Chem Commun*, **53**, 873 (2017).
16. J. Liang, X. Du, C. Gibson, X. W. Du and S. Z. Qiao, *Adv Mater*, **25**, 6226 (2013).
17. Y. Tang, B. L. Allen, D. R. Kauffman and A. Star, *J Am Chem Soc*, **131**, 13200 (2009).
18. N. Alexeyeva, E. Shulga, V. Kisand, I. Kink and K. Tammeveski, *J Electroanal Chem*, **648**, 169 (2010).

19. K. Gong, F. Du, Z. Xia, M. Durstock and L. Dai, *Science*, **323**, 760 (2009).
20. L. Lai, J. R. Potts, D. Zhan, L. Wang, C. K. Poh, C. Tang, H. Gong, Z. Shen, J. Lin and R. S. Ruoff, *Energ Environ Sci*, **5**, 7936 (2012).
21. D. Guo, R. Shibuya, C. Akiba, S. Saji, T. Kondo and J. Nakamura, *Science*, **351**, 361 (2016).
22. J. J. Li, Y. M. Zhang, X. H. Zhang, J. C. Han, Y. Wang, L. Gu, Z. H. Zhang, X. J. Wang, J. K. Jian, P. Xu and B. Song, *Acs Appl Mater Inter*, **7**, 19626 (2015).
23. M. Wang, Z. P. Wu and L. M. Dai, *J Electroanal Chem*, **753**, 16 (2015).
24. Z. Yi, Z. Zhang, S. Wang and G. Shi, *J Mater Chem A*, **5**, 519 (2017).
25. Y. Zheng, Y. Jiao, J. Chen, J. Liu, J. Liang, A. Du, W. Zhang, Z. Zhu, S. C. Smith, M. Jaroniec, G. Q. Lu and S. Z. Qiao, *J Am Chem Soc*, **133**, 20116 (2011).
26. Q. Han, B. Wang, Y. Zhao, C. G. Hu and L. T. Qu, *Angew Chem Int Edit*, **54**, 11433 (2015).
27. Z. J. Huang, F. B. Li, B. F. Chen and G. Q. Yuan, *Rsc Adv*, **5**, 14027 (2015).
28. Z. H. Wang, L. Chen, X. R. Du, G. J. Zou and X. L. Wang, *Rsc Adv*, **6**, 15605 (2016).
29. X. Q. Fan, L. X. Zhang, R. L. Cheng, M. Wang, M. L. Li, Y. J. Zhou and J. L. Shi, *Acs Catal*, **5**, 5008 (2015).
30. H. Q. Ma, Y. Li, S. Li and N. Liu, *Appl Surf Sci*, **357**, 131 (2015).
31. Y. S. Jun, E. Z. Lee, X. Wang, W. H. Hong, G. D. Stucky and A. Thomas, *Adv Funct Mater*, **23**, 3661 (2013).
32. C. Li, X. Yang, B. Yang, Y. Yan and Y. Qian, *Mater Chem Phys*, **103**, 427 (2007).
33. L.-L. Feng, Y. Zou, C. Li, S. Gao, L.-J. Zhou, Q. Sun, M. Fan, H. Wang, D. Wang and G.-D. Li, *Int J Hydrogen Energ*, **39**, 15373 (2014).
34. M. Shalom, S. Inal, C. Fettkenhauer, D. Neher and M. Antonietti, *J Am Chem Soc*, **135**, 7118 (2013).
35. J. R. Ran, T. Y. Ma, G. P. Gao, X. W. Du and S. Z. Qiao, *Energ Environ Sci*, **8**, 3708 (2015).
36. S. S. Shinde, A. Sami and J. H. Lee, *Chemcatchem*, **7**, 3873 (2015).
37. H. Q. Ma, S. Zhao, S. Li and N. Liu, *Rsc Adv*, **5**, 79585 (2015).
38. C. H. Lu, R. Y. Chen, X. Wu, M. F. Fan, Y. H. Liu, Z. G. Le, S. J. Jiang and S. Q. Song, *Appl Surf Sci*, **360**, 1016 (2016).
39. J. Li, B. Shen, Z. Hong, B. Lin, B. Gao and Y. Chen, *Chem Commun*, **48**, 12017 (2012).
40. S. M. Lyth, Y. Nabae, S. Moriya, S. Kuroki, M.-a. Kakimoto, J.-i. Ozaki and S. Miyata, *The Journal of Physical Chemistry C*, **113**, 20148 (2009).
41. Y. Sun, C. Li, Y. Xu, H. Bai, Z. Yao and G. Shi, *Chem Commun*, **46**, 4740 (2010).
42. S. Yang, X. Feng, X. Wang and K. Müllen, *Angewandte Chemie International Edition*, **50**, 5339 (2011).
43. J. Tian, R. Ning, Q. Liu, A. M. Asiri, A. O. Al-Youbi and X. Sun, *ACS Appl Mater Interfaces*, **6**, 1011 (2014).
44. X. Wang, L. Wang, F. Zhao, C. Hu, Y. Zhao, Z. Zhang, S. Chen, G. Shi and L. Qu, *Nanoscale*, **7**, 3035 (2015).

45. C. Y. Xu, Q. Han, Y. Zhao, L. X. Wang, Y. Li and L. T. Qu, *J Mater Chem A*, **3**, 1841 (2015).
46. M. Q. Wang, W. H. Yang, H. H. Wang, C. Chen, Z. Y. Zhou and S. G. Sun, *Acs Catal*, **4**, 3928 (2014).
47. H. B. Yang, J. Miao, S.-F. Hung, J. Chen, H. B. Tao, X. Wang, L. Zhang, R. Chen, J. Gao and H. M. Chen, *Science advances*, **2**, e1501122 (2016).
48. A. Ranganathan, V. Pedireddi and C. Rao, *J Am Chem Soc*, **121**, 1752 (1999).
49. J. Zhang, X. Chen, K. Takanahe, K. Maeda, K. Domen, J. D. Epping, X. Fu, M. Antonietti and X. Wang, *Angewandte Chemie International Edition*, **49**, 441 (2010).
50. X. Chen, Q. Liu, Q. Wu, P. Du, J. Zhu, S. Dai and S. Yang, *Adv Funct Mater* (2016).
51. S. N. Guo, Y. Zhu, Y. Y. Yan, Y. L. Min, J. C. Fan and Q. J. Xu, *Appl Catal B-Environ*, **185**, 315 (2016).
52. J. H. Lee, M. J. Park, S. J. Yoo, J. H. Jang, H. J. Kim, S. W. Nam, C. W. Yoon and J. Y. Kim, *Nanoscale*, **7**, 10334 (2015).
53. R. Jäger, P. E. Kasatkin, E. Härk and E. Lust, *Electrochem Commun*, **35**, 97 (2013).
54. A. J. Bard, L. R. Faulkner, J. Leddy and C. G. Zoski, *Electrochemical methods: fundamentals and applications*, Wiley New York (1980).

## Tables

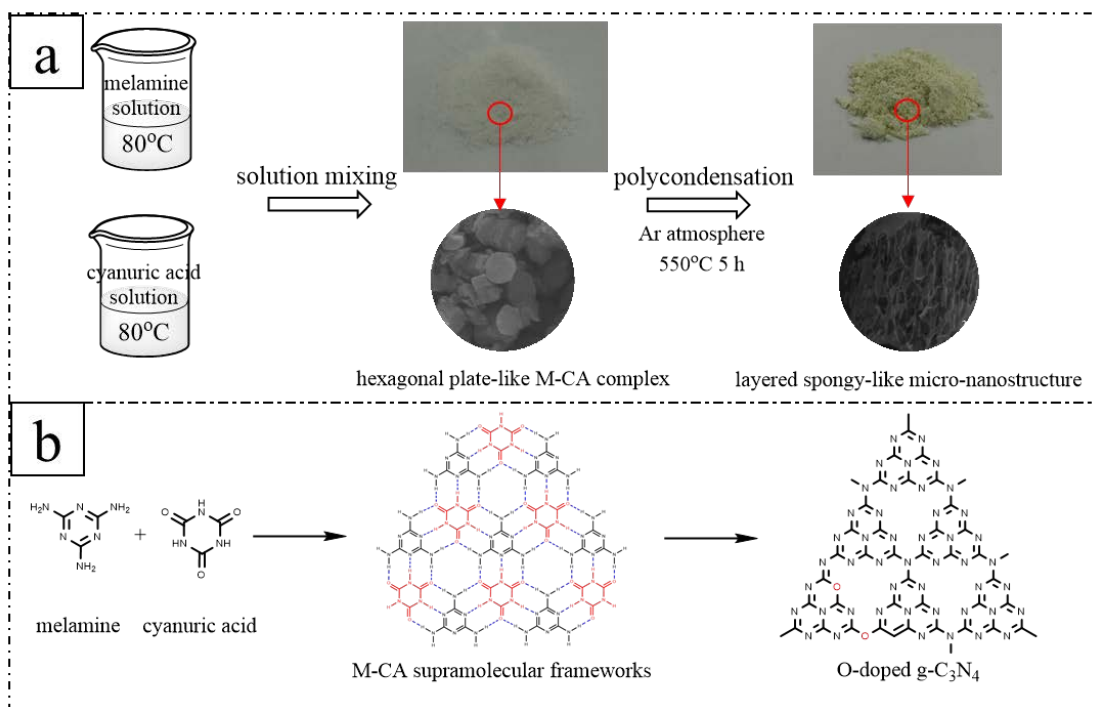
Table 1. The BET surface area, elemental content and band structure of gCN and O-gCN.

	Surface area	Elemental content (%)				Band structure (eV)		
	(m <sup>2</sup> g <sup>-1</sup> )	N	C	H	O	E <sub>g</sub>	CBM	VBM
gCN	23.2	63.06	35.43	1.5	0.18	2.79	-1.38	1.41
O-gCN	58.3	60.34	34.62	1.8	3.24	2.57	-1.21	1.36

Table 2. The contents of different C and N species for O-gCN and gCN from XPS analysis.

	C1s				N1s			
	C-C	C-O	N <sub>2</sub> -C=N	pyridinic- N	pyrrolic- N	quaternary- N	C <sub>6</sub> N <sub>7</sub>	N (sp <sup>2</sup> /sp <sup>3</sup> )
gCN	0.286	0.172	0.541	0.530	0.329	0.102	0.038	1.609
O-gCN	0.361	--	0.639	0.610	0.327	0.012	0.051	1.863

## Figures



Scheme 1. Schematic of the preparation process of O-gCN catalyst.

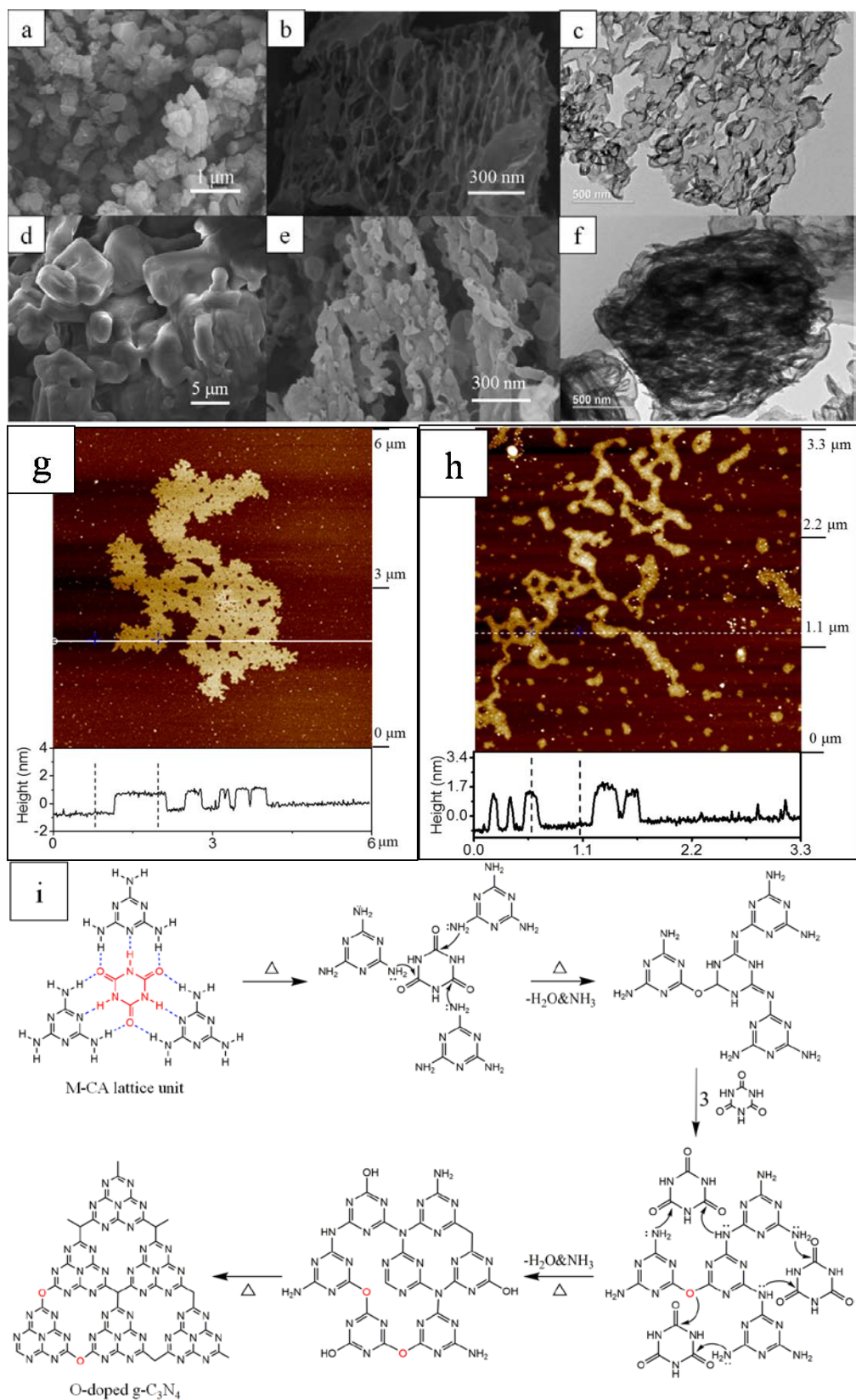


Figure 1. SEM images of M-CA complex (a) and O-gCN (b), TEM images of O-gCN (c), SEM images of M-CA mixture (d) and gCN (e), TEM images of gCN (f), AFM images of M-

CA complex (g) and O-gCN (h), schematic of the possible reaction mechanism for O-gCN  
(i).

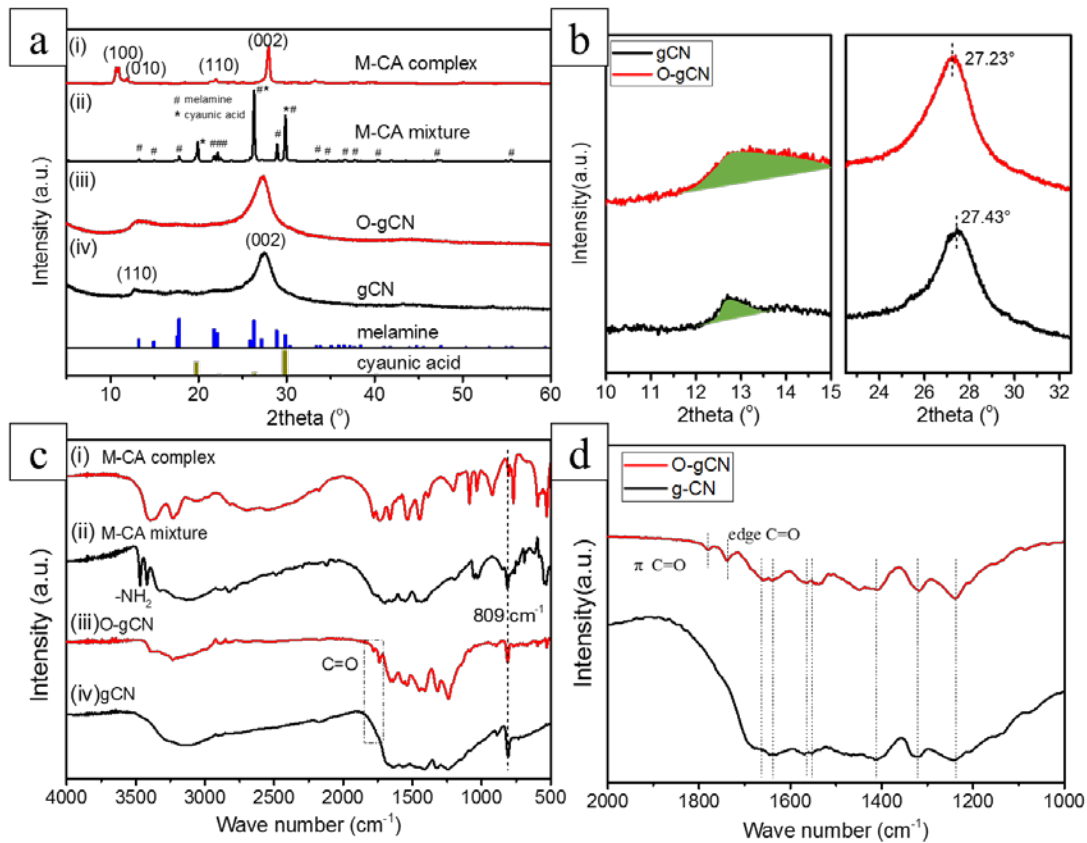


Figure 2. (a) XRD patterns of M-CA complex, M-CA mixture, O-gCN and gCN, (b) close observation of XRD patterns at (110) and (002) crystal facet for O-gCN and gCN, (c) FTIR spectra of M-CA complex, M-CA mixture, O-gCN and gCN, (d) close observation of FTIR spectra from 1000 to 2000 cm<sup>-1</sup> for O-gCN and gCN.

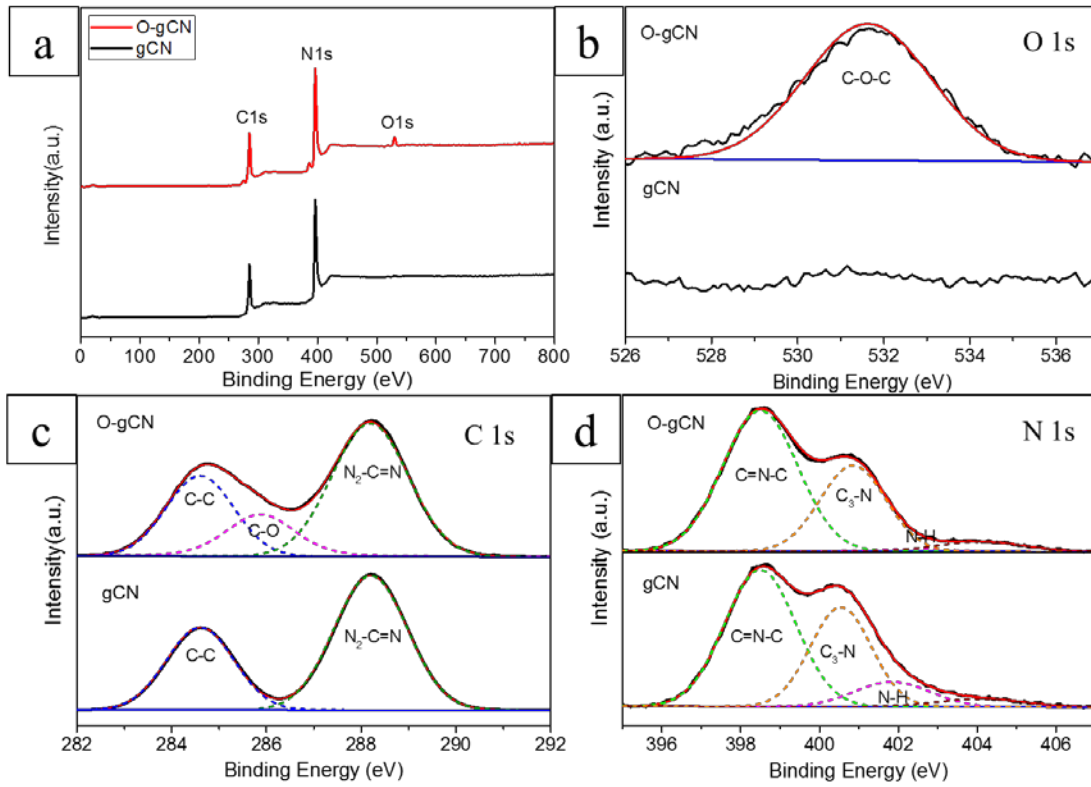


Figure 3. XPS spectra of O-gCN and gCN materials (a) survey of the sample, (b) O 1s, (c) C 1s, (d) N 1s.

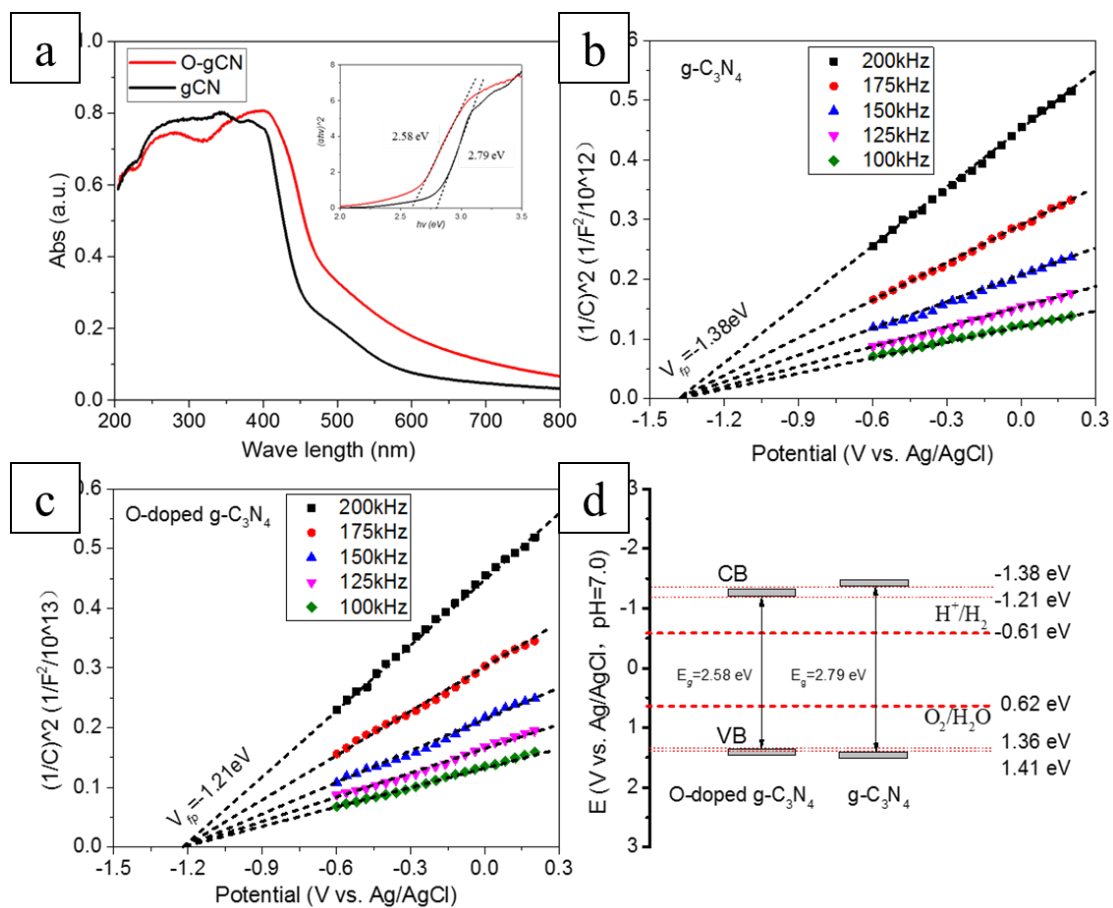


Figure 4. (a) DRS spectra and Tauc plots (inset) of O-gCN and gCN, (b) Mott–Schottky plots of O-gCN, (c) Mott–Schottky plots of O-gCN, (d) bandgap structures of O-gCN and gCN.

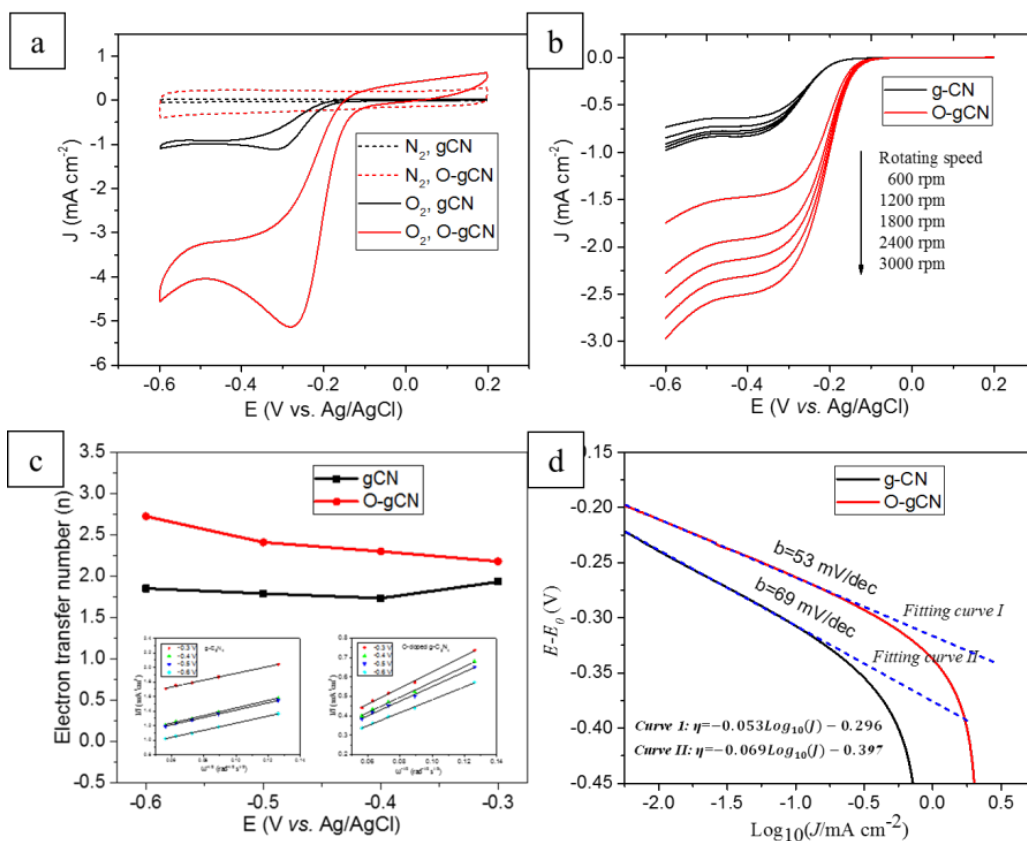


Figure 5. (a) CVs of gCN and O-gCN, (b) LSVs of gCN and O-gCN at different rotating rates, (c) the variation of electron transfer number at different potentials, (d) Tafel plots of gCN and O-gCN.

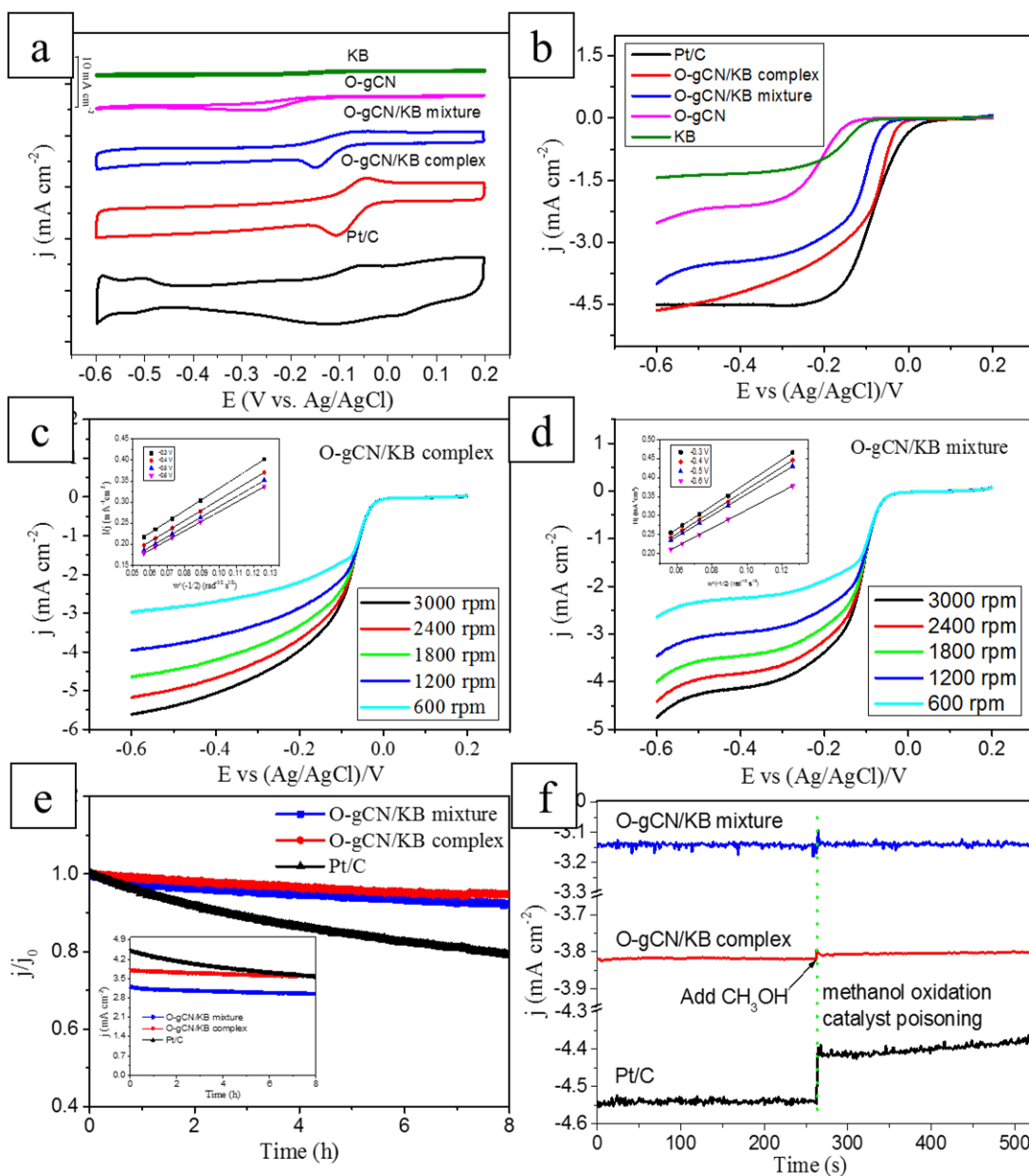


Figure 6. (a) CVs of various electrocatalysts. (b) LSVs of various electrocatalysts at 1800 rpm. (c) LSVs of O-gCN/KB mixture at different rotating rates and corresponding Koutecky-Levich plots at different potentials, (d) LSVs of O-gCN/KB complex at different rotating rates and corresponding Koutecky-Levich plots at different potentials, (e) the variation of relative current ( $J/J_0$ ) with time at  $-0.3$  V for various electrocatalysts, and inset represents their chronoamperometric responses, (f) the chronoamperometric responses with time at  $-0.3$  V in  $O_2$ -saturated 1 M KOH solution without methanol and with adding methanol.